Nonlinear traveling waves in rotating Rayleigh-Bénard convection: Stability boundaries and phase diffusion

Yuanming Liu and Robert E. Ecke

Condensed Matter and Thermal Physics Group and Center for Nonlinear Studies, Los Alamos National Laboratory,
Los Alamos, New Mexico 87545

We present experimental measurements of a sidewall traveling wave in rotating Rayleigh-Bénard convection. The fluid, water with Prandtl number about 6.3, was confined in a 1-cm-high cylindrical cell with radius-to-height ratio $\Gamma = 5$. We used simultaneous optical-shadowgraph, heat-transport, and local temperature measurements to determine the stability and characteristics of the traveling-wave state for dimensionless rotation rates $60 < \Omega < 420$. The state is well described by the one-dimensional complex Ginzburg-Landau (CGL) equation for which the linear and nonlinear coefficients were determined for $\Omega = 274$. The Eckhaus-Benjamin-Feir-stability boundary was established and the phase-diffusion coefficient and nonlinear group velocity were determined in the stable regime. Higher-order corrections to the CGL equation were also investigated. [S1063-651X(99)03204-3]

PACS number(s): 47.20.Bp, 47.32.−y, 47.54.+r

I. INTRODUCTION

Amplitude equations have formed the basis for much of the study of pattern-forming nonlinear systems [1]. For stationary bifurcations, the Ginzburg-Landau equation has proved very successful in quantitatively describing experimental data [2]. Its complex generalization, the complex Ginzburg-Landau (CGL) equation, has been one of the key generic equations for the description of *time-dependent* states in pattern-forming systems [1]. The nonlinear stability of pattern-forming traveling waves was investigated theoretically by Benjamin and Feir and by Newell [3,4] and has many features of the Eckhaus instability in stationary patterns [5]. Although the theory and numerical simulation of the CGL equation are very well developed [1,6–9], quantitative analysis of experimental data for a supercritical bifurcation has been sparse [10–12]. Other experimental systems that have exhibited features of the Eckhaus-Benjamin-Feir (EBF) instability are binary-mixture convection [13,14] and traveling finger patterns [15] although neither could be fit quantitatively into the CGL framework partially because of the subcritical nature of the primary bifurcation. Here, we present detailed comparison of experimental data from a nonlinear pattern-forming traveling wave observed in rotating Rayleigh-Bénard convection (RBC) with predictions based on the CGL equation. A brief report of this comparison was published previously [16].

The CGL equation in one spatial dimension describes the behavior of slow spatial and temporal modulations of plane waves with frequency ω_c and wave number k_c. The complex amplitude A in terms of modulation frequency ω and modulation wave number q obeys the CGL equation:

$$\tau_0(\partial_t A + s\partial_x A) = \epsilon(1 + ic_0)A + \xi_0^2(1 + ic_1)\partial_{xx}A$$
$$- g(1 + ic_3)|A|^2A, \quad (1)$$

where all the coefficients are real, τ_0 is the time scale, ξ_0 is the spatial scale, ϵ is the linear bifurcation parameter, and g is the nonlinear parameter. The coefficients c_i control the dependence of the frequency on k and ϵ. Viewed from the perspective of a controlled perturbation expansion of a more complicated partial differential equation, higher-order terms can be important for any physical realization of the equation. We describe these below. In certain regions of parameter space, the amplitude-equation description can be reduced to an equation for the phase field where the pattern wave number is the gradient of that phase. In that case the amplitude is slaved to the phase because amplitude perturbations relax much more quickly than the phase distortions.

The physical system of interest is Rayleigh-Bénard convection with rotation about a vertical axis. A series of experiments [16–20] using heat-transport measurements and simultaneous shadowgraph visualization and linear-stability analysis [21–23] have established that there is a sidewall traveling wave that exists as the first state unstable with respect to the conduction state provided the rotation rate is high enough. This work has also shown that the traveling-wave state has many characteristics of the CGL equation including a supercritical primary bifurcation. Further, there is a unique direction of the traveling wave, opposite to the rotation direction, with no associated counterpropagating wave. Thus a single CGL equation is sufficient to describe the system. It was also found that the variation in parameter values for the effective CGL equation is not adequate to bring the system into the very interesting regime where exotic hole solutions are possible [11,12]. This latter regime arises when the stable wave number band is close to vanishing, i.e., when the Newell criterion is satisfied [4].

The parameters controlling rotating convection are the Rayleigh number $R = g\alpha d^3\Delta T/\nu\kappa$ (acceleration of gravity g; thermal expansion coefficient α; temperature difference ΔT across the fluid layer of height d; kinematic viscosity ν; thermal diffusivity κ) and the dimensionless rotation rate $\Omega = 2\pi f d^2/\nu$. The bifurcation parameter is $\epsilon = R/R_c(\Omega) - 1$ where $R_c(\Omega)$ is the critical Rayleigh number for the onset of convection. Properties of thermal convection can also be af-
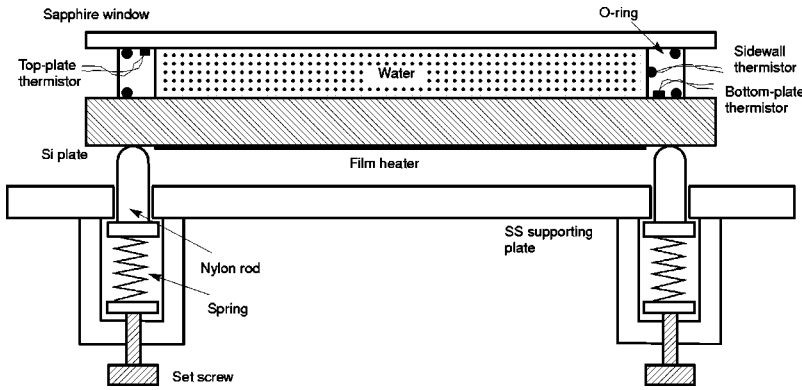
FIG. 1. Schematic illustration of the Rayleigh-Bénard convection cell.

fected by the Prandtl number $Pr \equiv \nu/\kappa$ which is 6.3 for the fluid used in this experiment (water) and the cell geometry characterized by the aspect ratio $\Gamma \equiv r/d$. In these experiments $\Gamma = 5$.

The paper starts in Sec. II with a description of the experimental apparatus and the procedures for obtaining data. In Sec. III, we present the characterization of the sidewall traveling-wave state and the determination of the coefficients in an amplitude-equation formalism. The stability of states with wave number k to long-wavelength Eckhaus-Benjamin-Feir instability is described in Sec. IV and results on phase dynamics are presented in Sec. V. We conclude with some remarks about future work in Sec. VI.

II. EXPERIMENTAL PROCEDURE

The rotating apparatus was described in detail elsewhere [24]. The cell assembly is schematically shown in Fig. 1. The top plate of the convection cell was a 1/8-in.-thick, 5-in.-diameter, optical-quality sapphire window. The bottom plate was a 3/8-in.-thick, 5-in.-diameter silicon plate which was polished with a mirror finish to one or two wavelengths over the whole surface. The silicon plate does not corrode in water and has good thermal and mechanical properties. The sidewall was 0.72-cm-thick plexiglass which defined a fluid layer with a height of 1.00 cm and a radius of 5.00 cm with an aspect ratio $\Gamma = r/d = 5.0$. The top-plate temperature was regulated to better than 0.5 mK rms over long periods of time by temperature-regulated water jets. Constant heat current was supplied by a 4-in.-diameter film heater attached to the bottom of the silicon plate. The power input to the heater was obtained by a four-wire measurement. The cell was insulated, on all surfaces except the top plate, by closed-cell foam to prevent thermal losses due to radiation and conduction or convection by air. All electrical wires were fed into the rotating frame through a low-noise electrical slip ring. Rotation was provided by a microstepping motor through two gears and a timing belt. The rotation rate was fully controllable by computer and the maximum rotation rate used in the experiment was $f = 0.6$ Hz.

To ensure a uniform water layer, several assembly features were built into the convection cell. The sapphire window deforms under stress, so a special design allowed us to adjust the stress on the window *in situ*, thereby achieving a uniformity of about 4 μm over the whole window area. Further, the nonuniformity was almost concentric so that the azimuthal uniformity needed in our experiment on sidewall

convection modes was considerably better than the overall uniformity. The bottom plate sat on three nylon rods set in a stainless-steel support. The nylon rods had spherical heads to allow point contact with the silicon plate and thus minimize heat loss. They were also spring loaded with tension independently adjustable by set screws. The parallelism between the bottom of the silicon plate and the top of the sapphire plate was fine tuned through the set screws and measured by a dial indicator to within 10 μm. The total uniformity of the water layer height was estimated to be better than 0.3%.

The top- and bottom-plate temperatures were measured by an average of three evenly spaced thermistors. The thermistors were mounted in the sidewall within the O rings, and were in poor thermal contact with the wall, but in good contact with the bottom surface of the sapphire window and the top surface of the Si plate. A pair of thermistors were horizontally mounted in the sidewall at the midheight, about 10° apart, and with their tips flush with the wall's inner surface, to provide local temperature information. From the data measured by the pair, the amplitude, frequency, and mode number of the mode could be extracted.

In addition to the temperature measurements, we also employed simultaneous optical-shadowgraph measurements to obtain both local and global information about the traveling waves on both a qualitative and quantitative level. The shadowgraph optics are described in detail in Ref. [25], and were mounted in the rotating frame. Specifically, we used an achromatic collimating lens with a diameter of 5 in. and a focal length of 25 in., a 50-mm Nikon lens as the imaging lens, a Sharp laser diode operating below lasing as the point light source, and a Sony black-and-white charge coupled device (CCD) camera (model SSC-M354) with 512×480 resolution. The positions of the imaging lens and the camera were independently adjustable, allowing for control of the image magnification and shadowgraph sensitivity. Images were typically 350×350 pixels, which contained the whole cell of approximate size 330×330 pixels. The shadowgraph signal was obtained by pixel-by-pixel division $[I(x,y,t) - I_0(x,y)]/I_0(x,y)$ where $I_0(x,y)$ is the intensity of a background image taken well below onset and $I(x,y,t)$ is the intensity of an image taken above onset at time t. The center of the cell (x_0,y_0) was found in each image, and the signal for a traveling wall state $I(r,\theta,t)$ was obtained by both azimuthally and radially averaging in a window of $\Delta r = 0.01r_0$ and $\Delta \theta = 1°$, where r is the radius relative to (x_0,y_0), θ is the azimuthal angle, and $r_0 \approx 165$ is the radius of the cell. $I(r,\theta,t)$ depends sensitively on both the shape of

the image and (x_0,y_0). The shadowgraph optics were adjusted to obtain as round an image as possible, but the images were sometimes out of round by one or two pixels. We averaged the shadowgraph signal over $0.98r_0 \leq r \leq 0.99r_0$ to yield a smoother signal but the slight azimuthal asymmetry of the images and uncertainty in (x_0,y_0) could cause a systematic, artificial nonuniformity in $I(r,\theta,t)$. This nonuniformity was taken out when necessary by dividing $I(r,\theta,t)$ by its long-time average.

The experimental control parameters for rotating Rayleigh-Bénard convection are ΔT which is proportional to R and the physical angular rotation rate Ω_D represented in dimensionless form by the dimensionless rotation rate $\Omega \equiv \Omega_D d^2/\nu$. During the experiments, the top-plate temperature T_t was held constant at $T_t = 24.1 \, ^\circ$C, and the bottom-plate temperature (T_b) varied with the heat input. The fluid parameters used to compute dimensionless control parameters were evaluated at the mean cell temperature. For most measurements reported below, the rotation rate was fixed at $\Omega = 274$ ($\Omega_D = 2.512$ rad/s). For this rotation rate, the ratio of the centrifugal-to-gravitational force was about 0.03 so centrifugal effects can be ignored.

To prepare states with different wave numbers, we took advantage of transients which enabled us to generate traveling waves with $17 \leq m \leq 32$ at $\Omega = 274$. The basic idea is that lower (higher) rotation produces smaller (larger) wave number in both the bulk and sidewall modes relative to the sidewall wave number that is selected by quasistatically ramping ϵ at fixed Ω. The other factor is that at higher ϵ the bulk mode is present, which can affect the mode selected as the sidewall state. A typical scenario for generating different modes is as follows: For low modes, a bulk mode was stabilized at $\Omega = 68$ and $\epsilon \approx 1$, then Ω was increased to about 274 and ϵ was decreased to about 0.25, both at a quasistatic rate. For high modes, we generated a mode with $\Omega = 414$ at $\epsilon \approx 1$, then quickly (about 40 s) ramped Ω down to 274. The mode was initially suppressed by the rapid deceleration, and reappeared later with a higher mode number. The ability to prepare different mode numbers enabled us to determine the marginal-stability and the Eckhaus-Benjamin-Feir-stability boundaries. Once a state at a particular ϵ and Ω was generated, we waited at least five or six vertical thermal diffusion times $\tau_\kappa = d^2/\kappa = 680$ s before determining steady-state quantities.

III. EXPERIMENTAL RESULTS

A. Primary and secondary bifurcations

The first two bifurcations in this system are from conduction to sidewall-traveling-wave convection and then, at higher ϵ to a state with both sidewall and bulk convection. These bifurcations were previously identified and studied for convection cells with $\Gamma = 1$ [17,19] and $\Gamma = 2.5$ [20]. The best indication of these bifurcations is the heat transport which we present as the Nusselt number N which is the effective fluid conductivity normalized by the thermally diffusive fluid conductivity. For our convection cell with $\Gamma = 5.0$, we measured the Nusselt number as a function of ΔT for $\Omega = 68,136,205,274,344,414$. The results are plotted in Fig. 2 as a function of ϵ and have several distinct features.

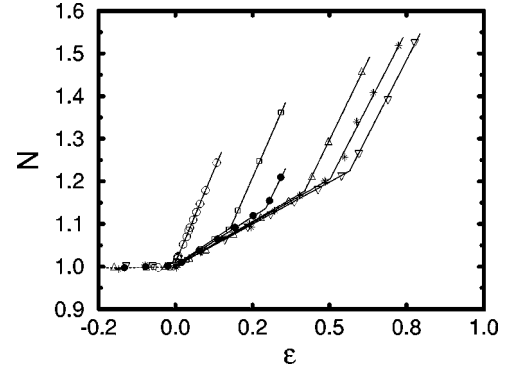FIG. 2. N vs ϵ for different dimensionless rotation rates: $\Omega = 68(\bigcirc)$, 136 ($\square$), 205 ($\bullet$), 274 ($\triangle$), 344 (*), and 414 ($\triangledown$). The lines show the linear dependence of N on ϵ for the sidewall traveling-wave and bulk states.

The change from $N = 1$ at $\epsilon = 0$ indicates the onset of convection. For most of the data sets, there is a linear section in N which is indicative of the sidewall mode. The second change in slope indicates the onset of bulk convection. As Ω decreases the first linear section also decreases in size so that for the lowest rotation rate $\Omega = 68$ the interval has decreased to zero and the transition is to coexisting sidewall and bulk convection. From the N measurements, the critical Rayleigh numbers for the sidewall mode and for the bulk convection state were determined and the results are shown in Fig. 3. Our results agree well with those measured previously [20], indicating that the initial bifurcation to the sidewall state depends only weakly on Γ. For the onset to bulk convection state, the critical R_b decreases slightly as Γ increases.

A further characterization of sidewall and bulk onsets is the critical frequency of the sidewall mode ω_c and critical wave numbers k_c and k_b for the sidewall and bulk states. Figure 4 shows the measured precession frequency ω_c at onset scaled by τ_κ. In the Ω range we studied, there is no noticeable difference between our results in a $\Gamma = 5.0$ cell and the results for $\Gamma = 2.5$ [20]. Calculations by Goldstein et al. support the experimental results that the frequency changes little with increasing Γ when $\Gamma > 1$ for moderately
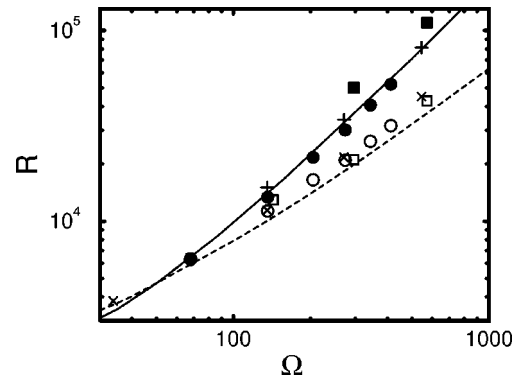

FIG. 3. $R_c(\bigcirc)$ and $R_b(\bullet)$ vs Ω for $\Gamma = 5$. For comparison, previous data for other values of Γ are shown: $\Gamma = 1.0$ (Zhong, Ecke, and Steinberg) $R_c(\square)$ and $R_b(\blacksquare)$; $\Gamma = 2.5$ (Ning and Ecke) $R_c(\times)$ and R_b (+). Also shown are Chandrasekhar's linear-stability calculation for a laterally infinite system (solid line) and calculation of Goldstein et al. for a $\Gamma = 1$ cell with insulating sidewalls (dashed line).
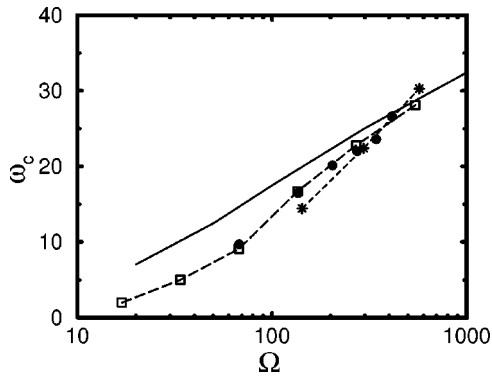
FIG. 4. Dimensionless precession frequency at onset ω_c as a function of Ω in cells with $\Gamma=5.0$ ($\bullet$), 1.0 (*, measured by Zhong, Ecke, and Steinberg), 2.5 ($\square$, measured by Ning and Ecke). The solid line is the calculation by Kuo and Cross for a planar wall state and the dashed lines are guides to the eye.

high Ω. In Fig. 5 the critical wave number is shown for the sidewall state and for the bulk state. Again the data are in good agreement with older data and with theoretical calculations. Note that k_b changes markedly with Ω whereas k_c is very weakly dependent on Ω.

B. Characterization of the sidewall traveling waves

The $\Gamma=5$ cell and the azimuthally periodic boundary conditions allowed us to prepare traveling-wave states with mode numbers ranging from $17\leqslant m\leqslant32$ at $\Omega=274$ ($\Omega_D=2.512$ rad/s). We used simultaneous heat transport, local temperature, and shadowgraph measurements to obtain the wave number, frequency, and amplitude of the sidewall states with these mode numbers. In our analysis we use either the azimuthal mode number m or the dimensionless wave number $k=m/\Gamma$ to parametrize the state. The frequency and, in general, any other quantity with units of time is made dimensionless by scaling with the thermal diffusion time τ_κ.

We expect, based on previous experiments [20] and on general principles [1], that there is a band of stable wave numbers for each ΔT and corresponding value of R bounded
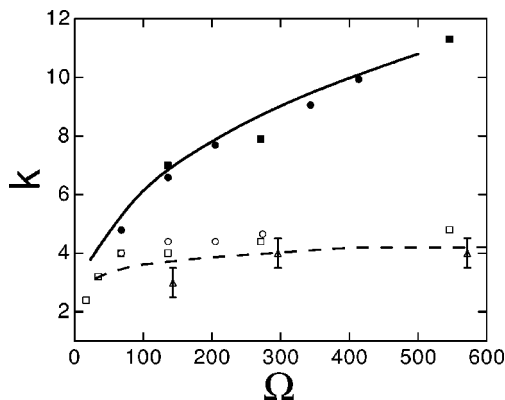

FIG. 5. Dimensionless critical wave numbers k_b and k_c vs Ω for bulk (solid symbols) and sidewall (open symbols): $\Gamma=5$ (circle), $\Gamma=2.5$ (squares), $\Gamma=1$ (triangles). The solid line is the linear-stability results of Chandrasekhar for the bulk state and the dashed line is the calculation by Kuo and Cross for a planar wall state.
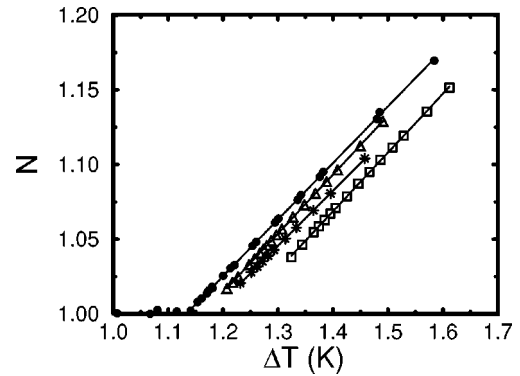

FIG. 6. Nusselt number N vs ΔT for different mode numbers: $m=23$ ($\bullet$), 27 ($\triangle$), 31 ($\square$), and 18 (*). The lines are least-squares linear fits to the data. Only data below the onset to bulk convection state are shown.

by the marginal-stability boundary. This boundary can be determined by measuring either the local mode amplitude or the global heat transport N as a function of k and R. Figures 6 and 7 show the Nusselt number N_k and the local squared amplitude A_k^2 versus ΔT for four selected mode numbers $m=18,23,27,31$ corresponding to $k=3.6,4.6,5.4,6.2$. N_k-1 and A_k^2 vary quite linearly with ΔT with slopes and zero intercepts that depend on k. For N_k the scaling is defined as

$$N_k-1=\alpha_k^{-1}(\Delta T-\Delta T_k),\qquad(2)$$

where ΔT_k is the value of ΔT for the marginal stability of a mode with wave number k and α_k has units of temperature. The dependence of A_k on k indicates that the local temperature probe has some instrumental response or radial-mode structure dependence as a function of k so we use N_k to determine the effective ''amplitude'' scaling. Over the range of ΔT shown, there is no statistically significant improvement in the fit by including a quadratic term, implying that the quadratic correction to the amplitude is small and will be neglected in the CGL-type analysis described below. We construct the marginal-stability curve from values of ΔT_k determined from measurements of N_k. The data are plotted in Fig. 8 and are well fit by a quadratic function
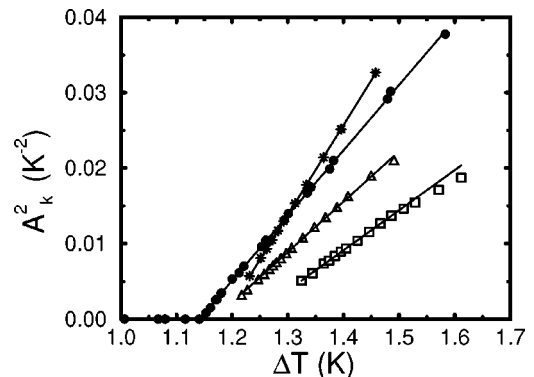
$$\Delta T_k=1.1374+0.0367(k-4.65)^2.\qquad(3)$$

FIG. 7. Sidewall probe amplitude A_k^2 vs ΔT for $m=23$ ($\bullet$), 27 ($\triangle$), 31 ($\square$), and 18 (*). The lines are least-squares linear fits to the data. Only data below the onset to bulk convection state are shown.

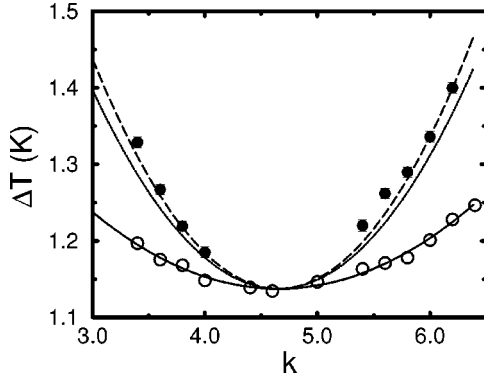FIG. 8. Marginal-stability boundary ($\bigcirc$) and EBF boundary ($\bullet$) for $\Omega = 274$. The solid line is a parabolic fit to the marginal-stability data. The dashed line is from the classic prediction for EBF boundary $\epsilon_E = 3\epsilon_M$. The dotted line is the curve obtained using $c_1 = 1.1$ and $c_3 = 0.6$ which yields $\epsilon_E = 2.8\epsilon_M$.

The minimum occurs at the critical wave number $k_c = 4.65$ with a corresponding onset value $\Delta T_c = 1.1374$ K which yields a critical Rayleigh number $R_c = 20\,850$. Fitting with a cubic correction in $(k - k_c)$ gives a cubic coefficient of -0.0012. For now we ignore the cubic correction. Having determined ΔT_c and k_c, we obtain scaled variables $\epsilon \equiv \Delta T/\Delta T_c - 1$ and $q = k - k_c$. In the remainder of this paper, k and q can be used interchangeably although we typically use q to label quantities such as $N_q, A_q, \alpha_q, \omega_q$, etc. We used the intercepts of the straight line fits to N_q to obtain the marginal-stability boundary but the slope of the lines α_q^{-1} in Eq. (3) also yields important information about CGL parameters. α_q is listed in Table I and plotted in Fig. 9. The small variation in α_q as a function of q represents a higher-order correction to the standard CGL equation as discussed below. We also define a quantity $\epsilon_q \equiv (\Delta T - \Delta T_k)/\Delta T_c = \epsilon + 1 - \Delta T_k/\Delta T_c$ which is zero along the marginal-stability boundary and which facilitates a description of the traveling-wave frequency and its later comparison with CGL-like equations.

The traveling-wave frequency ω_q plotted in Fig. 10 shows
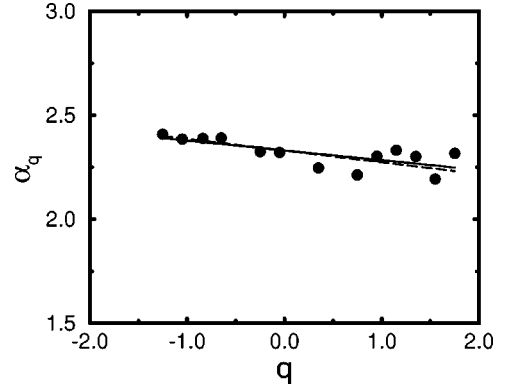

FIG. 9. Dimensionless coefficient α_q vs q. The solid line is a least-squares fit to the data. The dashed line is the best determination of the slope consistent with measurements of the nonlinear group velocity v_g.

deviations from linear dependence on ΔT over the same range where N_q and A_q^2 are very linear. Thus, we use quadratic fits to the ω_q data,

$$\omega_q = \omega_q^0 + \gamma_q \epsilon_q + \eta_q \epsilon_q^2, \tag{4}$$

where ω_q^0 is the frequency at the marginal instability for wave number q and is plotted in Fig. 11. The data are well represented by

$$\omega_q^0 = 21.96 - 2.65q + 0.136q^2, \tag{5}$$

where the constant term is the critical frequency $\omega_c = 21.96$. The frequency coefficients γ_q and η_q are plotted in Fig. 12 as functions of q and tabulated in Table I. These coefficients are reinterpreted below in the context of the CGL equation and its higher-order generalizations.

Before we proceed with further analysis of the data based on the CGL equation, we address the spatial structure of the modes in the radial direction. To do that we examine the radial profiles of states with different m using the optical-shadowgraph technique. Figure 13 displays four digitally en-

TABLE I. Marginal-stability boundary ΔT_k and corresponding ϵ_M, EBF boundary $\Delta T_k^E(\pm 0.007)$ and corresponding ϵ_E, and coefficients α_q, ω_q^0, γ_q, and η_q as functions of m and equivalently $k = m/\Gamma$ and $q = k - k_c$.

| m	k	q	ΔT_k (°C)	ϵ_M	$\Delta T_k^{(E)}$ (°C)	ϵ_E	α_q	ω_q^0	γ_q	η_q
17	3.4	-1.25	1.201	0.056	1.329	0.168	2.41	25.70	14(± 2)	$-13(\pm 3)$
18	3.6	-1.05	1.176	0.034	1.267	0.114	2.385	24.75	18	-22
19	3.8	-0.85	1.169	0.028	1.219	0.072	2.39	24.28	17	-14
20	4.0	-0.65	1.148	0.009	1.185	0.042	2.39	23.60	18	$-19(\pm 5)$
22	4.4	-0.25	1.139	0.001			2.325	22.51	22	-33
23	4.6	-0.05	1.134	-0.003			2.32	22.10	18	-10
25	5.0	0.35	1.146	0.008			2.245	21.08	24	$-22(\pm 5)$
27	5.4	0.75	1.164	0.023	1.220	0.073	2.215	20.20	23	-17
28	5.6	0.95	1.171	0.030	1.262	0.110	2.30	19.65	24	-13
29	5.8	1.15	1.178	0.036	1.290	0.134	2.33	18.97	25	-13
30	6.0	1.35	1.201	0.056	1.336	0.175	2.30	18.56	25	$-15(\pm 3)$
31	6.2	1.55	1.228	0.080	1.400	0.231	2.195	18.29	26	-14
32	6.4	1.75	1.247	0.096			2.315	17.61	27	-15
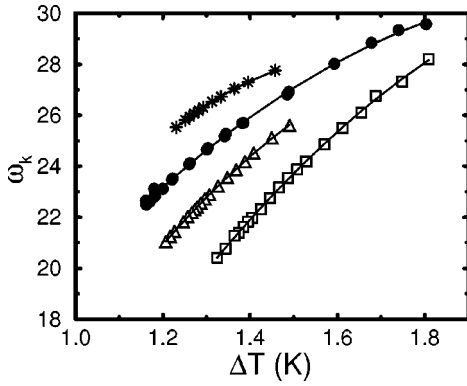
FIG. 10. Dimensionless frequency ω_k vs ΔT for mode number $m=23$ ($\bullet$ $k=4.6$), 27 ($\triangle$ $k=5.4$), 31 ($\square$ $k=6.2$), and 18 ($*$ $k=3.6$). The lines are least-squares quadratic fits to the data.

hanced shadowgraph images with modes 17, 23, 28, and 31 for $\epsilon_q \approx 0.23$. The second and even the third structure away from the wall are visible for all of these modes. Quantitatively, we characterize the radial distribution of the wave by calculating the standard deviation of shadowgraph intensity as a function of radius, $\sigma_I(r)$. The wave is separable into radial and azimuthal functions so that in the linear shadowgraph regime, we have

$$I(\theta, r) = 1.0 + \sqrt{2}\sigma_I(r)\sin(m\theta) \propto T_0 + T(r)\sin(m\theta) \quad (6)$$

so $\sigma_I(r)$ is directly proportional to temperature amplitude. Figure 14 shows $\sigma_I(r)$ for four selected modes ($m=17,23,28,31$) at constant $\epsilon_q \approx 0.19$. The position of the second peak moves further from the wall for higher mode numbers. It also moves further from the wall at higher ϵ at a constant mode number, as illustrated in Fig. 15. The dependence of the position on the mode number and ϵ is summarized in Fig. 16. There is no evidence that the radial structure is a necessary degree of freedom to consider in our analysis, which assumes a one-dimensional wave in the azimuthal direction and thus we ignore it in future discussion.

C. Description of the complex Ginzburg-Landau equation

The one-dimensional (1D) CGL equation, Eq. (1), was used successfully to describe some of the experimental re-
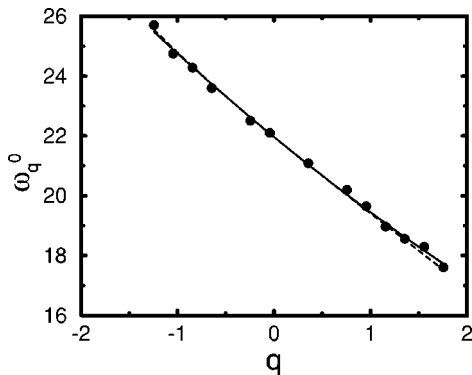

FIG. 11. Dimensionless frequency ω_q^0 vs q. The solid line is a least-squares quadratic fit to the data. The dashed line shows an additional cubic correction consistent with measurements of the nonlinear group velocity v_g.
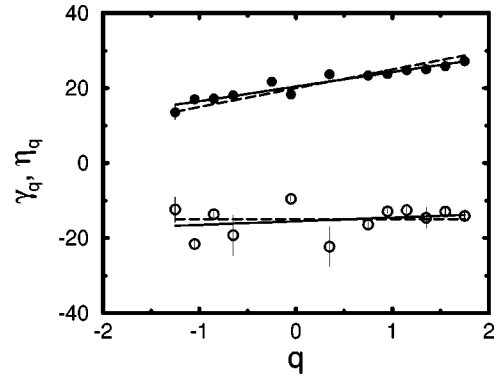

FIG. 12. Dimensionless coefficients γ_q and η_q vs q. Solid lines are least-squares fits to the data. Dashed lines are the best determination of the slope from comparison with all sets of data.

sults for a $\Gamma=2.5$ convection cell [20] and was proposed theoretically [22] for the weakly nonlinear traveling waves in rotating convection. Here we write a more general equation (denoted HOCGL for higher-order CGL) which includes some higher-order terms in a perturbation expansion of the rotating convection wall mode. These will be important in accounting for differences between the experimental results and the pure CGL equation

$$\tau_0(\partial_t A + s\partial_x A) = \epsilon(1+ic_0)A + \xi_0^2(1+ic_1)\partial_{xx}A$$
$$- g(1+ic_3)|A|^2 A + h(1+id_1)\partial_{xxx}A$$
$$+ j(1+id_2)\partial_x A|A|^2 - iw|A|^4 A. \quad (7)$$

In order to keep track of signs properly we now define the correspondence between the experiments and the CGL form: the coordinate x is the azimuthal angle taken to be positive in the counterclockwise direction as viewed from above. The sense of rotation is also counterclockwise so rotation is posi-
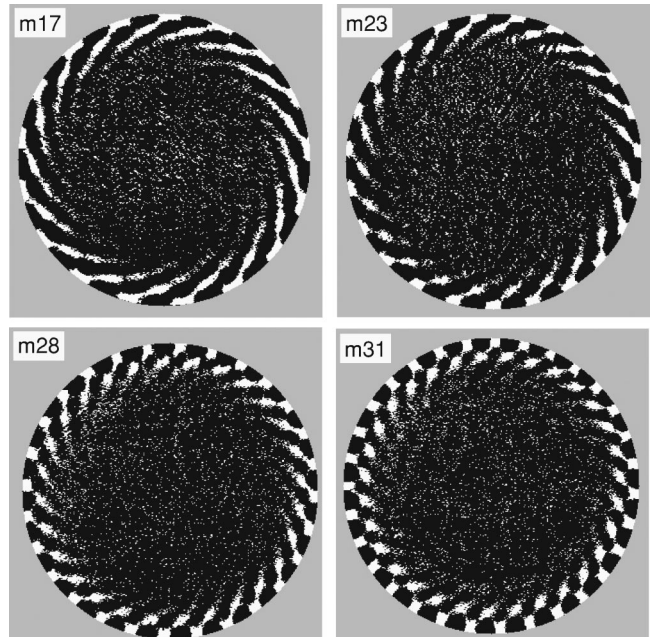

FIG. 13. Shadowgraph images for $m=17$ ($q=-1.25$, $\epsilon_q=0.22$, $\epsilon=0.27$), $m=23$ ($q=-0.05$, $\epsilon_q=0.22$, $\epsilon=0.22$), $m=28$ ($q=0.95$, $\epsilon_q=0.23$, $\epsilon=0.26$), and 31 ($q=1.55$, $\epsilon_q=0.27$, $\epsilon=0.35$).
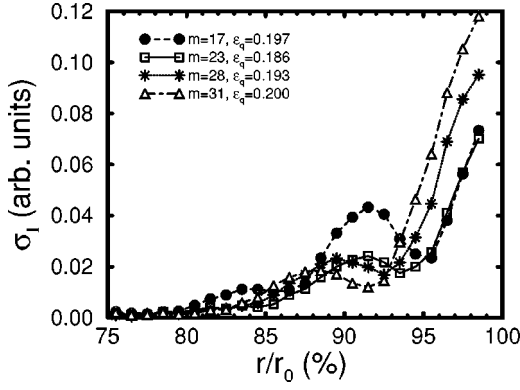
FIG. 14. Radial profile of root-mean-square shadowgraph intensity at constant $\epsilon_q \approx 0.195$ for mode 17 ($\bullet$ $q=-1.25$), 23 ($\square$ $q=-0.05$), 28 (* $q=0.95$), and 31 ($\triangle$ $q=1.55$). The lines are guides to the eye.

tive. The wave propagates opposite the rotation direction with negative phase velocity but the group velocity is positive. Thus a spatially uniform demodulated plane-wave solution takes the form

$$A(x,t)=A_q \exp[i(qx+\widetilde{\omega}t)], \qquad (8)$$

where $\widetilde{\omega}=\omega_k-\omega_c$ is the frequency difference from the critical frequency ω_c. We now plug this homogeneous solution into the CGL equation, Eq. (1), and also into the HOCGL equation, Eq. (7), which yields

$$i\tau_0(\widetilde{\omega}+sq)=\epsilon(1+ic_0)+\xi_0^2(1+ic_1)(-q^2)$$
$$-g(1+ic_3)|A_q|^2, \qquad (9)$$

$$i\tau_0(\widetilde{\omega}+sq)=\epsilon(1+ic_0)+\xi_0^2(1+ic_1)(-q^2)$$
$$-g(1+ic_3)|A_q|^2-ih(1+id_1)q^3$$
$$+ij(1+id_2)q|A_q|^2-iw|A_q|^4. \qquad (10)$$

For a homogeneous solution one can separate the real and imaginary parts to get for CGL

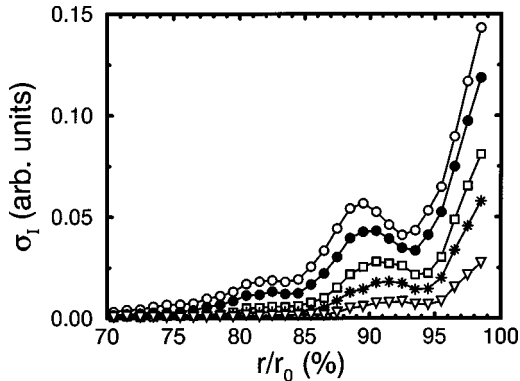
FIG. 15. Radial profile of root-mean-square shadowgraph intensity for mode 23 ($q=-0.05$) at $\epsilon_q=0.405, 0.313, 0.222, 0.150,$ and 0.0784, from top to bottom. At high ϵ, as many as four peaks are visible. The second peak from the wall extends further into the cell's interior as ϵ increases. The lines are guides to the eye.
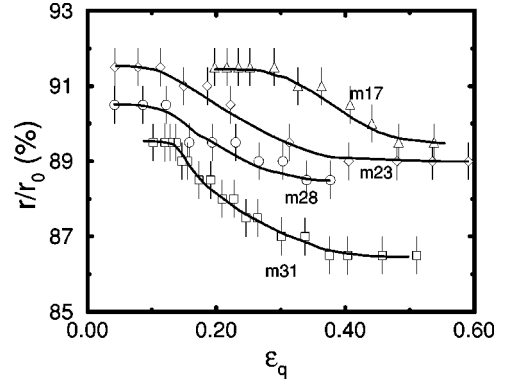

FIG. 16. The radial position of the second peak of the shadowgraph intensity away from the sidewall as a function of ϵ_q for different mode numbers indicated in the figure. The solid lines are guides to the eye.

$$0=\epsilon-\xi_0^2q^2-g|A_q|^2, \qquad (11)$$

$$\tau_0(\widetilde{\omega}+sq)=c_0\epsilon-c_1\xi_0^2q^2-gc_3|A_q|^2 \qquad (12)$$

or for Eq. (7)

$$0=\epsilon-\xi_0^2q^2+hd_1q^3-(g+jd_2q)|A_q|^2, \qquad (13)$$

$$\tau_0(\widetilde{\omega}+sq)=c_0\epsilon-c_1\xi_0^2q^2-(gc_3-jq)|A_q|^2-hq^3-w|A_q|^4. \qquad (14)$$

Solving for $|A_q|^2$ and $\widetilde{\omega}$ for CGL yields

$$|A_q|^2=\frac{\epsilon-\xi_0^2q^2}{g}=\frac{\epsilon_q}{g}, \qquad (15)$$

$$\widetilde{\omega}=-sq+\tau_0^{-1}[(c_0-c_3)\epsilon_q+(c_0-c_1)\xi_0^2q^2], \qquad (16)$$

where $\epsilon_q\equiv\epsilon-\xi_0^2q^2$ (this is equivalent to the previous definition in terms of ΔT_k) and for higher-order CGL

$$|A_q|^2=\frac{\epsilon-\xi_0^2q^2+hd_1q^3}{g+jd_2q}=\frac{\epsilon_{q_3}}{g+jd_2q}, \qquad (17)$$

$$\widetilde{\omega}=-sq+\tau_0^{-1}\left[\left(c_0-\frac{gc_3-jq}{g+jd_2q}\right)\epsilon_{q_3}+(c_0-c_1)\xi_0^2q^2 \right.$$
$$\left.-h(1+c_0d_1)q^3-\frac{w}{(g+jd_2q)^2}\epsilon_{q_3}^2\right]$$
$$=-sq+(c_0-c_1)\xi_0^2q^2/\tau_0-h(1+c_0d_1)q^3/\tau_0$$
$$+\gamma_q\epsilon_{q_3}+\eta_q\epsilon_{q_3}^2, \qquad (18)$$

where $\epsilon_{q_3}\equiv\epsilon-\xi_0^2q^2+hd_1q^3$.

To compare with experiment, we evaluate these expressions in several limiting cases. For fixed q, the dependence is just on ϵ_q or equivalently ϵ_{q_3} whereas along the marginal-stability curve, $|A_q|=0$ and one has

$$\epsilon_M = \xi_0^2 q^2, \quad \widetilde{\omega}_q = -sq + \frac{\xi_0^2}{\tau_0}(c_0 - c_1)q^2, \qquad (19)$$

$$\epsilon_M = \xi_0^2 q^2 - h d_1 q^3,$$

$$\widetilde{\omega}_q = -sq + \frac{\xi_0^2}{\tau_0}(c_0 - c_1)q^2 - \frac{h(1 + c_0 d_1)}{\tau_0}q^3. \qquad (20)$$

From our previous determination of the dependence of N_q and ω_q on q and ϵ_q, we can determine many of the CGL coefficients (or combinations thereof) and the higher-order correction terms:

$$\xi_0 = \left(-\frac{\partial^2 \epsilon_q / \partial q^2 |_{q=0}}{2} \right)^{1/2} = \left(\frac{\partial^2 \Delta T_q / \partial q^2 |_{q=0}}{2\Delta T_c} \right)^{1/2} = 0.179, \qquad (21)$$

$$s = -\left. \frac{\partial \widetilde{\omega}_q(\epsilon_q = 0)}{\partial q} \right|_{q=0} = 2.65, \qquad (22)$$

$$c_0 - c_1 = \frac{\tau_0}{2\xi_0^2} \left. \frac{\partial^2 \widetilde{\omega}_q(\epsilon_q = 0)}{\partial q^2} \right|_{q=0} = 0.136\tau_0/\xi_0^2 = 4.2\tau_0, \qquad (23)$$

$$c_0 - c_3 = \tau_0 \left. \frac{\partial \widetilde{\omega}_q(q=0)}{\partial \epsilon_q} \right|_{\epsilon_q=0} = \gamma_0 \tau_0 = 20.4\tau_0, \qquad (24)$$

$$h d_1 = \frac{1}{6} \left. \frac{\partial^3 \epsilon_{q_3}}{\partial q^3} \right|_{q=0} = 0.001, \qquad (25)$$

$$j + j d_2 c_3 = \left. \frac{g\tau_0 \partial \gamma_q}{\partial q} \right|_{q=0} = 3.9 g\tau_0, \qquad (26)$$

$$w = -\frac{\tau_0 g^2}{2} \left. \frac{\partial^2 \omega_q}{\partial \epsilon_{q_3}^2} \right|_{q=0} = -g^2 \eta_0 \tau_0 = 15 g^2 \tau_0. \qquad (27)$$

The nonlinear coefficients require a normalization of heat transport [20] which we take to be

$$N - 1 = |A|^2 \frac{(2\Gamma - 1)}{\Gamma^2} = 0.36|A|^2 \qquad (28)$$

for $\Gamma = 5$ so that

$$g = \frac{0.36}{\Delta T_c} \alpha_0, \qquad (29)$$

$$j d_2 = \frac{0.36}{\Delta T_c} \left. \frac{d\alpha_q}{dq} \right|_{q=0}, \qquad (30)$$

which yields $g = 0.74$ and $j d_2 = -0.015$. Knowing g, we get $j + j d_2 c_3 = 2.9\tau_0$ and $w = -g^2 \eta_0 \tau_0 = -0.55(-15)\tau_0 = 8\tau_0$. A few terms are difficult or impossible to obtain from steady-state data at fixed q or $\epsilon_q = 0$. In particular, determination of τ_0 requires a transient measurement and the cubic q dependence of ω_q^0 is too small to allow h to be resolved
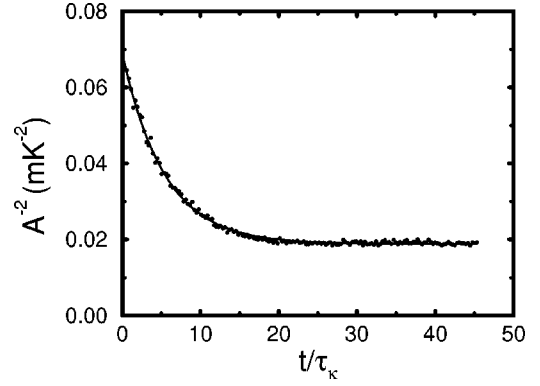

FIG. 17. Inverse squared amplitude A^{-2} vs time for $m = 23$ ($q = -0.05$) and $\epsilon = 0.001$. Solid line is fit to Eq. (33).

directly. Also, some of the coefficients are only determined in pairs and can only be deconvolved through transient measurements, c_3 being the principal example.

The measurement of transients in this system is complicated by competing time scales which are not always conveniently separated. The primary example of this is the measurement of τ_0 which we obtained from transient measurements of A_q using the side thermistors. The time scales involved are the fluid thermal relaxation time τ_κ and the convection roll relaxation time $\tau_\kappa \tau_0 / \epsilon$. In order for the amplitude equation to be valid, ϵ must have reached a stationary value which happens in several τ_κ. So one has the condition that $\tau_0 / \epsilon \geq 2$ or $\epsilon \leq \tau_0 / 2 \approx 0.01$. Thus, it is difficult to achieve enough resolution in ϵ to determine τ_0 accurately compared with, for example, convection in helium mixtures where τ_0 is ten times larger [26]. Another difficulty is that using the local probe to measure amplitude, which is necessary to achieve sufficient precision, assumes a uniform-amplitude state. As we see below, phase and amplitude distortions can exist and may be important. Despite these problems one can get some indication of the relaxation time through transient measurements.

We first show the relaxation expected for the CGL equation. We take $q = 0$ and assume that there are no spatial modulations of the state. The latter assumption may not be strictly valid but is difficult to test experimentally in the range of ϵ of interest. The transient-relaxation solution [27] for the amplitude and frequency of a spatially uniform state is

$$\tau_0 \partial_t A_0 = \epsilon A_0 - g A_0^3, \qquad (31)$$

$$\tau_0 \widetilde{\omega} = \epsilon c_0 - g c_3 A_0^2, \qquad (32)$$

which can be solved analytically for $A_0(t)$,

$$A_0(t) = \left[\frac{1}{A_0^2(\infty)} + \left(\frac{1}{A_0^2(0)} - \frac{1}{A_0^2(\infty)} \right) \exp\left(-\frac{2t}{(\tau_0/\epsilon)} \right) \right]^{-1/2}, \qquad (33)$$

where $A_0(\infty) = (\epsilon/g)^{1/2}$. An example of the transient measurement is plotted in Fig. 17 for mode number 23. ϵ increased in this measurement and approached $\epsilon = 0.001$ after about $2\tau_\kappa$. Using many such measurements, we obtain τ^{-1} as a function of ϵ which we plot in Fig. 18. If things were
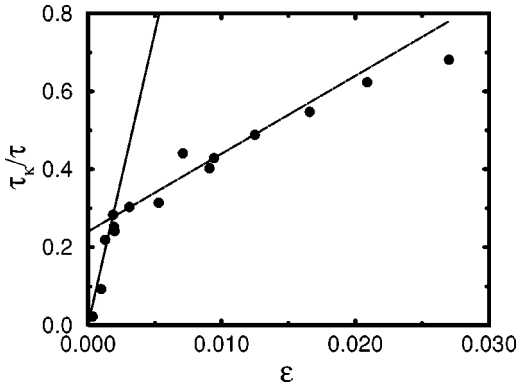
FIG. 18. Dimensionless inverse lifetime τ_κ/τ vs ϵ for determination of τ_0. The solid line is a linear fit to the data at small ϵ corresponding to $\tau_0 = 0.007$. The dashed line is a linear fit to data at intermediate ϵ with $\tau_0 = 0.050$.

well behaved, τ^{-1} would be linear in ϵ with slope τ_0. From these data, however, it is difficult to determine unambiguously the value of τ_0^{-1}. The data very near onset would suggest $\tau_0 \approx 0.007$ whereas the slope at higher ϵ implies $\tau_0 \approx 0.050$. Another piece of evidence is the apparent crossover towards $\tau \approx 1$ corresponding to the fluid thermal relaxation time τ_κ. Since this crossover should occur for $\tau_0 \lesssim 2\epsilon$, this would indicate that $\tau_0 \approx 0.030$. This value corresponds closely to the value $\tau_0 = 0.027$ obtained for a $\Gamma = 2.5$ convection cell at $\Omega = 544$. Finally, numerical results [22] for a plane traveling-wave wall mode suggest that τ_0 increases slightly with decreasing Ω. On the basis of the evidence presented here we take the value $\tau_0 = 0.030$ but clearly there is substantial uncertainty in this result. In the results presented below this will not be important for analysis of the EBF boundary or the nonlinear group velocity. It will be important in comparisons of the phase-diffusion coefficient between experiment and theory. We will discuss this more below.

IV. ECKHAUS-BENJAMIN-FEIR INSTABILITY

The marginal-stability boundary determined previously does not reveal the stability of the nonlinear states with wave number q. The nonlinear-stability boundary for traveling waves is the analog of the Eckhaus-stability boundary for stationary patterns which we denote here as the Eckhaus-Benjamin-Feir instability [1,3,4,11]. A coarse determination of this boundary is obtained from analysis of N_q as a function of ΔT. In Fig. 6, the data do not extend to $N = 1$ as would be expected from linear stability. Instead there are gaps in ΔT where there is no stable state for that q. These gaps do not, however, provide an accurate method for determining the boundary because the time to nucleate a defect pair can be very long. Therefore, we measure the nucleation time for defects as a function of ϵ and extrapolate to infinite nucleation time or equivalently to zero growth rate. This procedure, discussed in detail below, allows us to experimentally determine the EBF boundary (ΔT_E or ϵ_E) as a function of q, which is plotted in Fig. 8. The dashed line, $\epsilon_E = 3\epsilon_M$ with $\epsilon_M(q) = \xi_0^2 q^2$, is a very good approximation to the experimental data, and is obtained by setting $c_3 = 0$ in the theoretical equation for EBF derived from the CGL equation
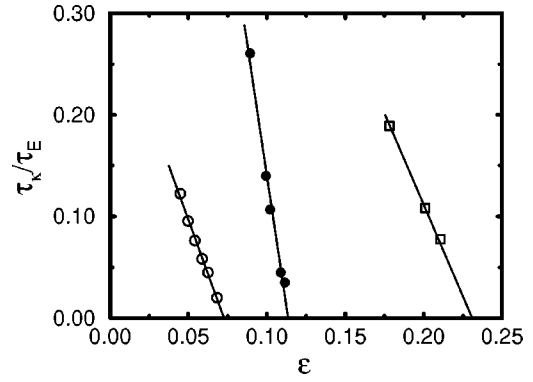

FIG. 19. Inverse lifetime τ_κ/τ_E of an EBF-unstable state vs ϵ for mode numbers 18 ($\bullet$ $q = -1.05$), 27 ($\bigcirc$ $q = 0.75$), and 31 ($\square$ $q = 1.55$).

$$\epsilon_E = \frac{2(1+c_3^2)+1+c_1 c_3}{1+c_1 c_3}\epsilon_M. \tag{34}$$

This does not necessarily imply $c_3 = 0$ as other combinations of c_1 and c_3 yield similar curves, specifically the case $c_1 = c_3$. The dotted curve in Fig. 8 shows the case for $c_1 = 1.1$ and $c_3 = 0.6$ where c_3 was suggested by a pulse-propagation technique [28] in a similar convection cell. The differences are small.

The detailed procedure we used to obtain the EBF-stability boundary is as follows: We prepared a traveling-wave state with a desired m at a high ϵ_i for which the state was stable. We then waited typically three to four hours to allow the state to equilibrate after which we suddenly decreased ϵ to slightly below the estimated ϵ_E. The unstable state had a finite lifetime τ_E before it generated or annihilated rolls through the formation of space-time dislocations, which is the signature of the EBF instability. τ_E was measured for different ϵ_f starting with a state at a constant high ϵ_i which was chosen for two reasons. First, when a state with mode number m was prepared, it was typically nonuniform in space with sizable variation in local wave number. In order to prevent these local variations from becoming EBF unstable, ϵ_i was chosen to be higher than ϵ_E for adjacent mode numbers $m \pm 1$. Second, at high ϵ_i the state equilibrates faster, allowing more rapid acquisition of data. In Fig. 19, we plot the normalized inverse lifetime τ_κ/τ_E versus ϵ for states with $m = 18,27,31$ ($q = -1.05,0.75,1.55$). ϵ_E is determined by linearly fitting the data and finding the intercept $\tau_\kappa/\tau_E = 0$. This procedure is significantly better than the simplest approach of determining the boundary by picking the last value which shows a nucleation within the waiting time. An even better method would take into account the slightly different initial relaxation times until a constant ϵ is reached which depends on the final ϵ_f. It would also measure the exponential growth of the unstable mode rather than the time to dislocation nucleation which involves nonlinear saturation. This is considerably more difficult, is not likely to change the results much because the maximum variation in τ_E caused by variations in ϵ_f are ten times less than the shortest τ_E, and has not been tried here.

Using optical shadowgraph, we observed the dynamics of the EBF transition. Figure 20 shows a sequence of shadowgraph images which correspond to different stages in the
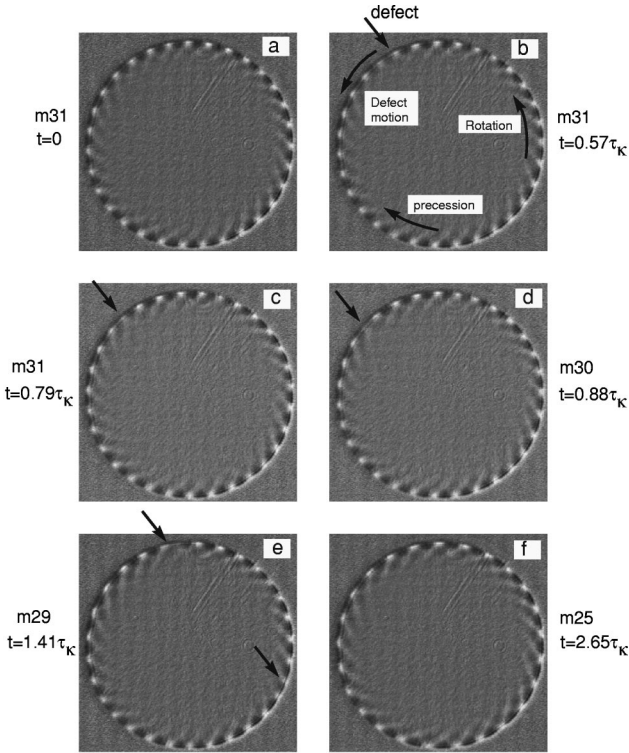
FIG. 20. Selected time sequence of shadowgraph images corresponding to the space-time plot in the next figure. These images are not digitally enhanced, only background division has been performed. The time lapse for the image in (a) is about $4.0\tau_\kappa$ from $t=0$ in the next figure and is used as the time reference in this figure. (a) shows an almost uniform state with $m=31$ ($q=1.55$). Images (b), (c), and (d) show a propagating dislocation and transition to the state of $m=30$ ($q=1.35$). Image (e) shows two dislocations occurring simultaneously. Image (f) shows the final state of $m=25$ ($q=0.35$) after all the transitions.

EBF transition. The state started with $m=31$ ($q=1.55$) and equilibrated to one with $m=25$ ($q=0.35$) after multiple dislocation nucleations. The directions of rotation, precession of the waves, and propagation of wave-number and amplitude distortions (labeled defect motion) are shown in the figure. Figure 21(a) shows a space-time plot of all the data represented in Fig. 20 and illustrates the convection roll annihilation through EBF instability. The data in Fig. 21(a) were taken from shadowgraph images, e.g., Fig. 20, along a circumference at 99% of the cell radius with a width of about 2% where the traveling wave had almost maximum amplitude. The horizontal axis is the azimuthal angle which increases counterclockwise in the direction of rotation. The time advances from bottom to top with a total duration of about 6000 s or $9.7\tau_\kappa$. The convection rolls traveled clockwise, counter to the direction of rotation. The EBF transition is marked by the development of space-time dislocations, six of which are visible in Fig. 21(a). To get a better picture of the nucleation of these defects, we demodulate the image to obtain the modulus (amplitude) and phase of the state. We then determine the local wave number as the gradient of the phase field. The gray-scale-coded amplitude and wave number are shown in Figs. 21(b) and 21(c), respectively, where dark (light) corresponds to smaller (larger) amplitude or wave number. The distortions in amplitude and wave number
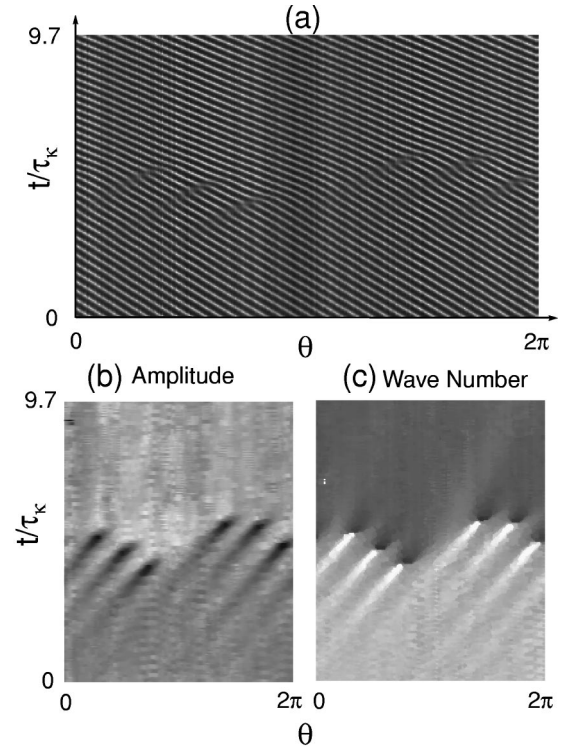

FIG. 21. Angle-time plot of traveling wave with mode number $m=31$ ($q=1.55$) for (a) azimuthal shadowgraph intensity, (b) demodulated amplitude, (c) demodulated wave number. Counter-propagating space-time dislocations and the resulting EBF transition can be seen.

which lead to dislocation nucleation propagate in the direction of rotation and are n-fold periodic in x (n is the azimuthal distortion mode number equivalent to the azimuthal mode number m for the undemodulated state). They are also characterized by amplitude depression and roll compression (increased local wave number) leading up to the dislocation nucleations. Immediately after a dislocation forms, the wave number decreases dramatically as indicated in Fig. 21(c) by the sudden change from bright to dark near each dislocation nucleation. For the case $q<0$, the amplitude decreases in a similar fashion up to the dislocation nucleation but the rolls dilate (decreased wave number). This latter scenario is illustrated in Figs. 22(a)–22(c) which show space-time plots of roll creation through EBF transition starting with $m=17$ ($q=-1.25$) and ending with $m=21$ ($q=-0.45$). For all EBF transitions that we studied with $17\le m\le32$, the amplitude was always depressed near the dislocation, whereas the wave was stretched when $q<0$ to accommodate an extra roll pair and compressed when $q>0$ which squeezes out an extra roll pair.

An interesting feature of the EBF transition shown in Fig. 21 is the large number of dislocations that are nucleated and the large change in wave number that results. As noted earlier, the time for nucleation of dislocations is a strong function of the distance of the final state below the EBF boundary. For the $m=31$ data shown in the figure, $\epsilon_E\approx0.231$ whereas ϵ_f was 0.16 which yields $\Delta\epsilon=\epsilon-\epsilon_E\approx-0.07$. For the data in Fig. 22, $\epsilon_E=0.168$ and ϵ_f was 0.11 so that $\Delta\epsilon\approx-0.06$. The relatively large difference in both of these examples resulted in fast dynamics and multiple dislocations.
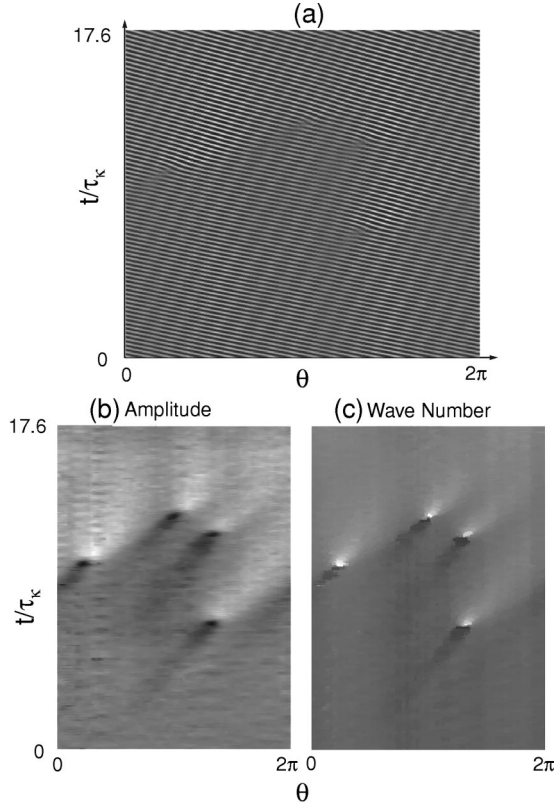
FIG. 22. Angle-time plot of traveling wave with mode number $m=17$ $(q=-1.25)$ for (a) azimuthal shadowgraph intensity, (b) demodulated amplitude, (c) demodulated wave number. Counter-propagating amplitude distortions which terminate in space-time dislocations which are signatures of the EBF transition can be seen.
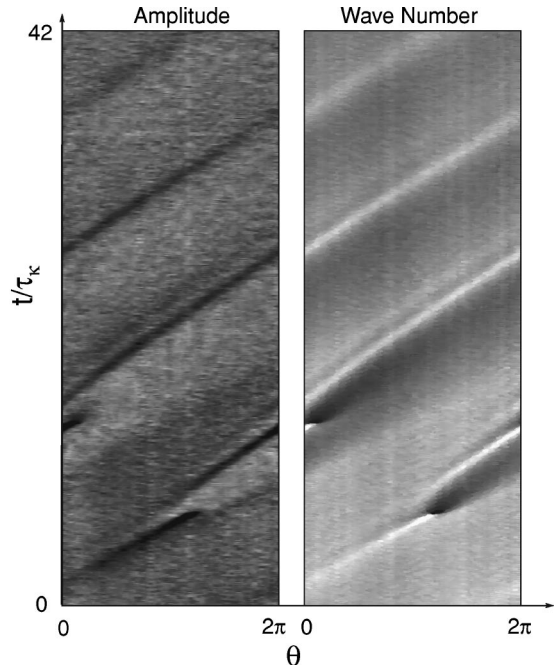

FIG. 23. Angle-time plot of amplitude (left) and wave number (right) for the EBF transition for $m=31$ $(q=1.55)$ at $\Delta\epsilon_E = -0.030$. See text for more detail.
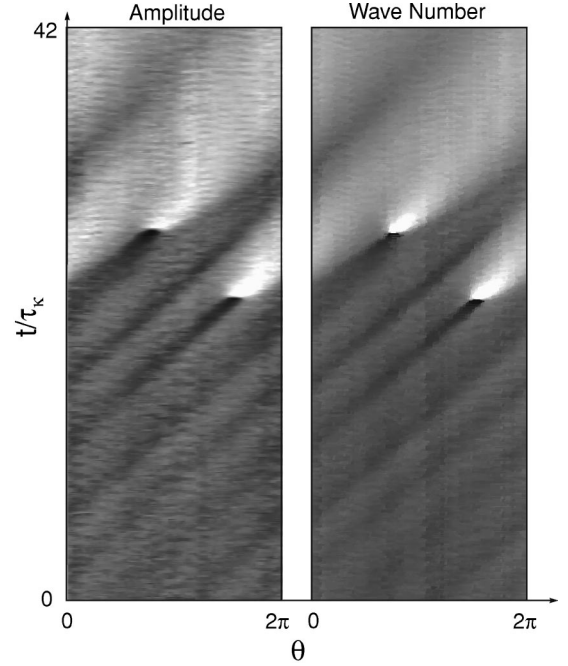

FIG. 24. Angle-time plot of demodulated amplitude (left) and demodulated wave number (right) for the EBF transition with $m = 17$ $(q=-1.25)$ at $\Delta\epsilon_E = -0.005$. See text for more detail.

As ϵ approached ϵ_E from below, the dynamics became slower and the number of transitions became smaller, from multiple transitions to a single transition. Figures 23 and 24 show space-time plots of the amplitude and wave-number evolution for a slower dynamics. The initial states of $m = 31$ and $m = 17$ were prepared at $\epsilon_i = 0.35$ and 0.27, respectively, and then were quickly lowered to $\epsilon_f = 0.201$ and 0.164 corresponding to $\Delta\epsilon = -0.03$ and -0.004. In Fig. 23, the space-time plot starts about $2.2\tau_\kappa$ after the initial decrease in ϵ, and the first transition to $m=30$ occurred $7.0\tau_\kappa$ later. In Fig. 24, the space-time plot started about $26\tau_\kappa$ after the decrease in ϵ, and the first transition to $m=18$ occurred $22\tau_\kappa$ later. There are several differences in the dislocation nucleations in these examples. For the sequence in Fig. 23, the first dislocation nucleation which resulted in a state with $m = 30$ generated another localized perturbation which led to the second transition to $m=29$. In the other example, Fig. 24, the two nucleations arise from a threefold periodic distortion of which only two produce defects while the other decays. Additional perturbations of amplitude and wave number after the second transitions in both figures decayed and vanished as the states equilibrated within the stable wave-number band. This decay is a measure of the diffusion of phase and amplitude governed by a slow phase dynamics. In the next section, we make quantitative measurements of the decay rate and nonlinear group velocity in the stable wave-number regime. We will also explain the nucleation of single versus multiple defects within the context of the phase dynamics description.

V. PHASE DYNAMICS

The modulus of the complex amplitude in Eq. (1) relaxes on a time scale τ_0/ϵ. In some regions of parameter space,
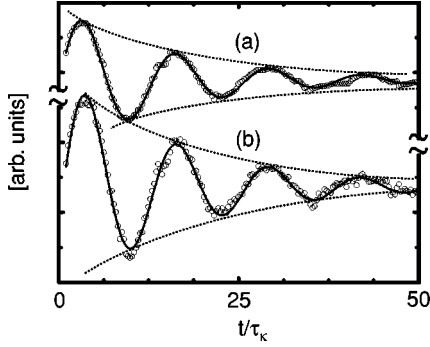
FIG. 25. Demodulated (a) frequency and (b) amplitude of the phase modulation for $m=27$ ($q=0.85$) and $\epsilon=0.26$. Solid (dashed) curves show fits to a decaying periodic function (envelope).

phase (or wave-number) distortions relax much more slowly. In that case, the modulus is slaved to the phase so that to linear order and for long-wavelength modulations the phase ϕ obeys a diffusion equation [11] for each q:

$$\partial_t\phi+v_g\partial_x\phi=D_2\partial_{xx}\phi+\Omega_0\partial_{xxx}\phi+D_4\partial_{xxxx}\phi, \quad (35)$$

where $p=\partial_x\phi$ and the coefficients D_2, Ω_0, and D_4 depend on q and ϵ. This equation is technically valid near the EBF boundary where $D_2\approx0$ but we will explore its usefulness in describing properties of phase distortions in the entire band of stable states. For that analysis we will ignore spatial derivatives higher than second order in Eq. (35). Corrections and limitations will be discussed below. For now let us assume that some initial perturbation exists which, for the periodic boundary conditions applicable here, can be written in terms of modes with period n corresponding to wave number $p=n/\Gamma$,

$$\phi(x,t)=\sum_{n=1}^{\infty} a_n e^{\sigma t+i(px-\tilde{\nu}t)}. \quad (36)$$

Plugging this solution into Eq. (35) yields, for each n, relationships for the growth rate σ and the oscillation frequency $\tilde{\nu}$,

$$\sigma=-D_2 p^2=-D_2\frac{n^2}{\Gamma^2}, \quad (37)$$

$$\tilde{\nu}=-v_g p=-v_g\frac{n}{\Gamma}. \quad (38)$$

The resulting expression for σ explains the long-time behavior of states in Figs. 21 and 22: A single dislocation nucleation produces a localized disturbance in wave number made up of many modes with a distribution of n. Modes with $n>1$ are, however, damped out much faster (like n^2) than the $n=1$ mode, so that after a short time only the $n=1$ mode survives.

The rapid decay of higher modes gives us a useful technique with which to measure D_2 and v_g. Using our sidewall probe, we determine the local amplitude and frequency and obtain D_2 and v_g from their decay rate and oscillation fre-
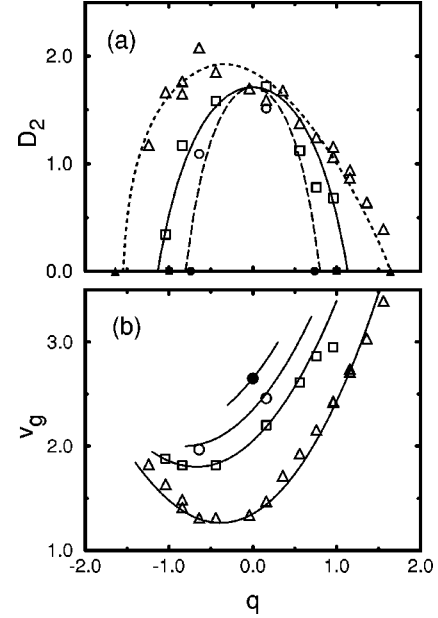

FIG. 26. (a) D_2 vs q for $\epsilon=0.26$ ($\triangle$), $\epsilon=0.12$ ($\square$), and $\epsilon=0.06$ ($\bigcirc$). Corresponding solid symbols are determination of the condition $D_2=0$ from location of the EBF-instability boundary. Solid and long-dashed curves are fits consistent with CGL predictions and experimental parameters. Short dashed line is guide to eye for data with $\epsilon=0.26$. (b) v_g vs q for same data as (a) with addition of $\epsilon=0$ linear group velocity s ($\bullet$). Solid lines are fits to data discussed in the text.

quency, respectively. In Fig. 25, we show the transient decay of the amplitude and the frequency distortions about the homogeneous state (we demodulate with the state at q and $\tilde{\omega}$). The initial states for different q are created by sequences of changes in rotation and heating rates to produce a spatially inhomogeneous state. The resulting data, collected after higher modes have decayed substantially, are fit with exponentially decaying sinusoidal functions which are also shown in the figure. The fits are typically excellent, implying that only a single $n=1$ mode is present. Sometimes the fits are poorer at short times, which indicates that higher modes have not decayed completely. One could measure the phase relaxation using the shadowgraph technique but the signal-to-noise ratio is not nearly as good as for the sidewall probe.

We measured D_2 and v_g for several different values of ϵ and for most of the available values of q as shown in Figs. 26(a) and 26(b). The values of D_2 can be compared with the predictions based on pure CGL,

$$D_2=\frac{\xi_0^2}{\tau_0}\left(1+c_1 c_3-\frac{2\xi_0^2 q^2(1+c_3^2)}{\epsilon_q}\right), \quad (39)$$

which is valid near q_E at which $D_2=0$. Expressions for other q away from q_E and incorporating higher-order corrections have not been calculated. For small $\epsilon\lesssim0.12$, D_2 roughly obeys the inverse parabolic form suggested above whereas for $\epsilon=0.26$, there are clear deviations as the data are highly asymmetric about $q=0$. A calculation for D_2 in a Taylor-Couette system yields very similar deviations [2,29]. In order to evaluate the theoretical prediction [11] for D_2, the coefficients must be determined completely. In particular, since

TABLE II. Coefficients in CGL equation and its higher-order generalization.

Coefficient	Value	Value (dimensionless)	Source
τ_0	$1\tau_0$	0.03	Figs. 17, 18
s	2.65	2.65	Fig. 11
ξ_0	0.179	0.179	Fig. 8
$c_0 - c_1$	$4\tau_0$	0.12	Fig. 11
$c_0 - c_3$	$20.4(\pm 0.4)\tau_0$	0.61	Fig. 12(a)
g	$0.74(\pm 0.05)$	$0.74(\pm 0.05)$	Fig. 9
h	$0.04\tau_0$	0.001	Fig. 26(b)
d_1	$0.025\tau_0^{-1}$	0.83	Figs. 8, 26(b)
j	$3.7\tau_0$	0.11	Figs. 12(a), 26(b)
d_2	$-0.005\tau_0^{-1}$	0.17	Fig. 9, 26(b)
w	$8\tau_0$	0.24	Fig. 12(b), 26(b)

we only have combinations of c_0, c_1, and c_3 and because τ_0 is poorly determined, it is difficult to do a direct comparison. Also, as shown below, a good understanding of the behavior of v_g requires the inclusion of significant higher-order effects. Those are unknown here so caution needs to be exercised in making comparisons. For the purposes of comparison, we take $c_1 = 1.1$, $c_3 = 0.6$ [30], and $\tau_0 = 0.03$ which yields the curves for $\epsilon = 0.06$ and 0.12. Given the uncertainties, the agreement is quite good. A better calculation is clearly called for as is a better determination of τ_0 and c_3.

The nonlinear group velocity v_g offers a better opportunity for comparison with higher-order CGL models. We rewrite Eqs. (16) and (18) in terms of fixed ϵ and q and differentiate with respect to q to obtain, respectively,

$$v_{g_0} = -s + 2\frac{\xi_0^2}{\tau_0}(c_3 - c_1)q, \tag{40}$$

$$
\begin{aligned}
v_{g_3} \approx v_{g_0} + \frac{1}{\tau_0}\Bigg[& \frac{(j + jd_2c_3)}{g}\epsilon + \frac{4w\xi_0^2 - 2jd_2(j + jd_2c_3)}{g^2}q\epsilon \\
& - 3\left(\frac{(j + jd_2c_3)\xi_0^2}{g} + (1 + c_3d_1)h\right)q^2 \\
& - \frac{6w}{g^3}(2jd_2\xi_0^2 - ghd_1)\epsilon q^2 \Bigg] \\
= & -s + b_1\epsilon + (b_2 + b_3\epsilon)q + (b_4 + b_5\epsilon)q^2, \tag{41}
\end{aligned}
$$

where the coefficients b_i can be determined from fits to the v_g data at different ϵ. The solid curves in Fig. 26(b) are obtained using the coefficients $b_i = 5, -1, 2.1, -0.55, -0.21$ which are slightly different from those reported earlier [16] and from a direct determination based on the coefficients obtained above. The present set is, however, within the error bars for the coefficients and the dashed curves in Figs. 9 and 12 show slopes implied by the fit. The differences are minute and within experimental uncertainty. The excellent agreement between the amplitude-equation description and the experimental data is startling. The only coefficient not obtainable from previous measurements that is determined by the v_g data is h although the final best estimate for the coefficients shown in Table II combines the direct measurements with the fit to the v_g data.

When we started our description of phase dynamics, we pointed out that a key assumption of this type of model is that the modulus of the amplitude is slaved to the slower phase field. The data in Fig. 25 support this slaving as, on a coarse scale, there is no visible delay between variations in amplitude and frequency (corresponding to wave-number distortions via the relationship $p = \tilde{\nu}/v_g$). On closer inspection, there is a discernible time delay of typically 100 s or about $0.15\tau_k$ with the amplitude lagging the phase oscillations. Thus, our measurements are consistent over a wide range of parameters with the assumptions of the theoretical models.

In addition to the dynamics of phase distortions in the stable band, the phase equation has important qualitative predictions about the growth of distortions in the EBF-unstable region. In Figs. 21, 22, and 24, there are multiple nucleations of dislocations arising from quite visible periodic amplitude and phase distortions. The explanation for why the system chooses to nucleate many dislocations with the resulting large change in q rather than producing a single dislocation can be found in an analysis of Eq. (35). When D_2 is positive, the higher-order term D_4 plays a secondary role. In the EBF-unstable regime, however, D_2 is negative and without a higher-order term, all phase distortions with any p become unstable. The presence of D_4 produces a band of unstable p with a maximum growth rate $\sigma_{max}(p_{max}) = 3D_2^2/4D_4$ with $p_{max} = \sqrt{-D_2/2D_4}$. As D_2 becomes negative upon crossing into the unstable region, p_{max} increases. Thus, for $\epsilon \approx \epsilon_E$ there should be only a single dislocation whereas for ϵ considerably below ϵ_E, the fastest growing mode corresponds to an n-fold distortion resulting in multiple dislocation nucleations. We have not studied this thoroughly but the trend is clearly consistent with this picture. In Fig. 27, we plot the number of periods n of the phase distortion versus the distance from the EBF boundary for several values of q. The increase in n is in qualitative agreement with the model but not with specific CGL calculations [11]. The independence of the ratio D_2/D_4 on τ_0 suggests that for this system expressions for D_2 and D_4 may not work very well. Further work on this aspect of the instability would be interesting especially if expressions could be derived for D_2 and D_4 from the higher-order forms of the CGL equation. Finally, the bounds on p appear to be such that the final wave number
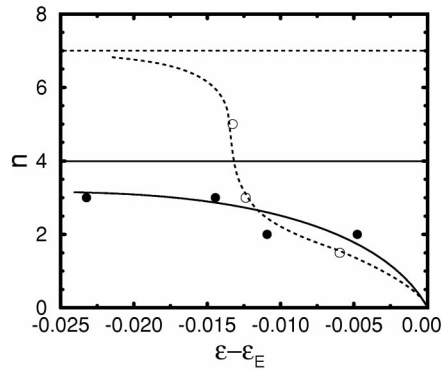
FIG. 27. Phase distortion periodicity n vs $\epsilon - \epsilon_E$ for $m = 30$, $q = 1.35$ (dashed curve) and $m = 27$, $q = 0.75$ (solid curve). The horizontal lines indicate the respective bounds on the distortion corresponding to taking the states back to the critical mode $m = 23$ ($q = -0.05$). The dashed and solid curves are guides to the eye.

is the critical one; we never observed a transition that reduced (increased) the wave number beyond k_c when starting from higher (lower) wave number. In principle the bound might be the opposite EBF wave number but our data are not sufficient to comment further on this point.

VI. CONCLUSION

We have explored in detail the ability of amplitude and phase equations of the complex Ginzburg-Landau type to describe experimental observations of nonlinear traveling waves in rotating Rayleigh-Bénard convection. The quantitative agreement between the experimental data and the theory is excellent and provides a detailed example of how the amplitude/phase-equation approach yields a striking and accurate description of a real physical experiment. The ability to select a discrete set of wave numbers as a consequence of the periodic boundary conditions of the physical system and thus to probe the q dependence of the amplitude and frequency is key to this investigation. The measurement of the phase-diffusion coefficient D_2 and the nonlinear group

velocity v_g for traveling waves is unique to this system because of its azimuthal periodicity. Overall, the data presented here provide the starting point for a set of future investigations of nonlinear traveling waves including interactions with external periodic and aperiodic spatial forcing, the possible observation of a geometric phase in dissipative systems [31], and the behavior of nonlinear waves without the restrictions imposed by periodic boundaries (i.e., breaking azimuthal periodicity). Unfortunately, the dependence of the experimentally determined coefficients in the CGL equation on rotation do not appear to encompass the interesting chaotic regime of Benjamin-Feir turbulence.

The only significant uncertainties in our analysis arise from poor measurements of the time constant τ_0 and the inability to independently determine the nonlinear coefficient c_3. We hope to better resolve these coefficients in future experiments using pulse-propagation techniques.

We hope that our measurements will provide motivation for further theoretical work on higher-order expansions and on better calculations of the phase-diffusion coefficient. Recently, calculations of the linear and weakly nonlinear stability of traveling wall modes in rotating convection have been performed [32] which make earlier calculations [22,23] more realistic. Also, theoretical work on the properties of the CGL equation in finite domains has shown interesting effects resulting from the existence of a single traveling-wave direction [6–9]. This latter case is realized experimentally by inserting a piece of metal foil along the inner wall of the convection cell, suppressing the wall mode, and breaking the azimuthal symmetry of the system. In that case, a unique wave number is selected and the convectively unstable regime does not seem to be accessible owing to the effects suggested by theoretical investigations [9]. This subject is planned to be the topic of a sequel to the present work [28].

[1] M. C. Cross and P. C. Hohenberg, Rev. Mod. Phys. **65**, 851 (1993).

[2] G. Ahlers, in *Lectures in the Science of Complexity*, SFI Studies in the Sciences of Complexity Vol. 1, edited by D. Stein (Addison-Wesley Longman, Redwood City, CA, 1989), p. 175.

[3] T. Benjamin and J. Feir, J. Fluid Mech. **27**, 417 (1967).

[4] A. Newell, *Envelope Equations*, Lectures in Applied Mathematics Vol. 15 (American Mathematical Society, Providence, RI, 1974).

[5] V. Eckhaus, *Studies in Nonlinear Stability Theory*, Springer Tracts in Natural Philosophy Vol. 6 (Springer-Verlag, Berlin, 1965).

[6] H. Müller, M. Lücke, and M. Kamps, Phys. Rev. A **45**, 3714 (1992).

[7] P. Büchel, M. Lücke, D. Roth, and R. Schmitz, Phys. Rev. E **53**, 4764 (1996).

[8] D. Roth *et al.*, Physica D **97**, 253 (1996).

[9] S. Tobias, M. Proctor, and E. Knobloch, Physica D **113**, 43 (1998).

[10] V. Croquette and H. Williams, Phys. Rev. A **39**, 2765 (1989).

[11] B. Janiaud, A. Pumir, D. Bensimon, V. Croquette, H. Richter, and L. Kramer, Physica D **55**, 269 (1992).

[12] N. Mukolobwiez, A. Chiffaudel, and F. Daviaud, Phys. Rev. Lett. **80**, 4661 (1998).

[13] P. Kolodner, Phys. Rev. A **46**, 1739 (1992); **46**, 6431 (1992).

[14] G. Baxter, K. Eaton, and C. Surko, Phys. Rev. A **46**, 1735 (1992).

[15] L. Pan and J. de Bruyn, Phys. Rev. E **49**, 2119 (1994).

[16] Y. Liu and R. E. Ecke, Phys. Rev. Lett. **78**, 4391 (1997).

[17] F. Zhong, R. Ecke, and V. Steinberg, Phys. Rev. Lett. **67**, 2473 (1991).

[18] R. E. Ecke, F. Zhong, and E. Knobloch, Europhys. Lett. **19**, 177 (1992).

[19] F. Zhong, R. Ecke, and V. Steinberg, J. Fluid Mech. **249**, 135 (1993).

[20] L. Ning and R. E. Ecke, Phys. Rev. E **47**, 3326 (1993).

[21] H. Goldstein, E. Knobloch, I. Mercader, and M. Net, J. Fluid Mech. **248**, 583 (1993).

[22] E. Kuo and M. C. Cross, Phys. Rev. E **47**, 2245 (1993).

[23] J. Hermann and F. Busse, J. Fluid Mech. **255**, 183 (1993).

[24] Y. Liu and R. E. Ecke (unpublished).

[25] J. R. de Bruyn, E. Bodenshatz, S. W. Morris, S. Trainoff, Y. Hu, D. S. Cannell, and G. Ahlers, Rev. Sci. Instrum. **67**, 2043 (1996).

[26] R. E. Ecke, H. Haucke, Y. Maeno, and J. Wheatly, Phys. Rev. A **33**, 1870 (1986).

[27] R. Deissler, R. E. Ecke, and H. Haucke, Phys. Rev. A **36**, 4390 (1987).

[28] R. E. Ecke (unpublished).

[29] H. Riecke, Ph.D. thesis, University of Bayreuth, Germany, 1980.

[30] Recent preliminary pulse-propagation experiments in a cell with broken azimuthal symmetry suggest a value $c_3 \approx 0.5$ but detailed analysis has not been done.

[31] A. Landsberg, Phys. Rev. Lett. **69**, 865 (1992).

[32] W. Choi, D. Prasad, R. Camassa, and R. E. Ecke (unpublished).